Dielectronic recombination data for dynamic finite-density plasmas

I. Goals and methodology

N. R. Badnell[1], M. G. O'Mullane[1], H. P. Summers[1], Z. Altun[2], M. A. Bautista[3], J. Colgan[4], T. W. Gorczyca[5], D. M. Mitnik[6], M. S. Pindzola[4], and O. Zatsarinny[5]

[1] Department of Physics, University of Strathclyde, Glasgow G4 0NG, UK
[2] Department of Physics, Marmara University, 81040, Ziverbey, Istanbul, Turkey
[3] Centro de Física, Instituto Venezolano de Investigaciones Científicas (IVIC), PO Box 21827, Caracas 1020A, Venezuela
[4] Department of Physics, Auburn University, Auburn, AL 36849, USA
[5] Department of Physics, Western Michigan University, Kalamazoo, MI 49008, USA
[6] Departamento de Física, FCEN, Universidad de Buenos Aires, Buenos Aires, Argentina

Abstract. A programme is outlined for the assembly of a comprehensive dielectronic recombination database within the generalized collisional–radiative (GCR) framework. It is valid for modelling ions of elements in dynamic finite-density plasmas such as occur in transient astrophysical plasmas such as solar flares and in the divertors and high transport regions of magnetic fusion devices. The resolution and precision of the data are tuned to spectral analysis and so are sufficient for prediction of the dielectronic recombination contributions to individual spectral line emissivities. The fundamental data are structured according to the format prescriptions of the Atomic Data and Analysis Structure (ADAS) and the production of relevant GCR derived data for application is described and implemented following ADAS. The requirements on the dielectronic recombination database are reviewed and the new data are placed in context and evaluated with respect to older and more approximate treatments. Illustrative results validate the new high-resolution zero-density dielectronic recombination data in comparison with measurements made in heavy-ion storage rings utilizing an electron cooler. We also exemplify the role of the dielectronic data on GCR coefficient behaviour for some representative light and medium weight elements.

Key words. atomic data – atomic processes – plasmas

1. Introduction

Dielectronic recombination (DR) is the dominant electron–ion recombination process in many astrophysical and laboratory plasmas. It plays an important role in determining both the level populations and the ionization balance of both high- and low-temperature non-LTE plasmas over a wide range of electron densities and its accurate description is key to spectral analysis (e.g. Judge et al. 1997; Lanzafame et al. 2002). Dielectronic recombination can be viewed as a two-step process. Firstly, a free electron excites an electron in an ion X^{+z}, say, and in the process transfers sufficient of its energy that it is captured into an autoionizing state of the ion X^{+z-1}. The process is reversible since the total energy of the system remains conserved. However, if an electron (either the captured electron or an electron in the parent core) then makes a spontaneous radiative transition that leaves the ion in a non-autoionizing (bound) state

then the recombination can be viewed as complete, at least in the low-density (coronal) limit. Dielectronic recombination can take place via many intermediate autoionizing states – indeed, entire Rydberg series. It was the significance of the effective statistical weight of so many available states that led Burgess (1964) to recognize the importance of dielectronic recombination in the first instance. A consequence of this is that a huge population structure model is required in principle for further progress. In astrophysics and fusion, the problem has usually been made manageable by simply summing over all final states so as to produce a total dielectronic recombination rate coefficient. In combination with radiative recombination, this is the effective recombination coefficient from the point of view of an ionization state only – the so-called "coronal picture". In this picture, excited-state populations are depleted exclusively by spontaneous radiative transitions and are small compared to those of ground states – with which they are in quasi-static equilibrium. Collisional processes are negligible, except with ground state targets. In turn, the ionization state

is determined by balancing the effective recombination rate of (the ground state of) X^{+z} against the collisional ionization rate of (the ground state of) X^{+z-1}.

For dynamic finite-density plasmas, there are therefore two critical limitations to the coronal approximation which must be addressed. Both require a re-appraisal of the strategy for computing dielectronic recombination, which is the objective of this paper. Firstly, from the atomic point of view, a dynamic plasma is one for which the timescale of change in plasma parameters (especially electron temperature, T_e, and electron density, N_e) is comparable with the lifetime of the metastable populations of its constituent ions. This situation is a concern, for example, for impurities near plasma contacted surfaces in fusion (Summers et al. 2002) and for active solar events (Lanza et al. 2001). The population of an ionization stage may no longer be assumed to be concentrated in the ground state of each ion. A significant population is found in the metastables, and they may not be in quasi-static equilibrium with the ground state. This means that such metastables are the starting point for recombination events, and so the time-evolution of their populations must be tracked in the same manner as for the ground states. We call this the generalized collisional–radiative (GCR) picture (Summers & Hooper 1983). Even if the metastable populations are in quasi-static equilibrium with the ground state, they are significant and so are still a source term for dielectronic recombination which cannot be ignored.

The second issue is that of finite-density effects. The coronal (zero-density limit) picture assumes that, following the two-step dielectronic recombination process, the resultant (non-autoionizing) excited-state (electron) radiatively cascades back down to the ground state without collisional disruption. At finite electron densities, this radiative cascade can be interrupted by further electron collisions which redistribute the population – in particular, ionization (possibly stepwise) out of excited states, which reduces the effective dielectronic recombination rate. Collisional–radiative modelling removes the limitations of the coronal model, but at the cost of much more elaborate excited-state population calculations. These in turn require much more detailed dielectronic recombination data, and in an easily accessible form. The onset of these density effects on the "post-DR" population structure depends markedly on ion charge, but can be significant even at electron densities as low as $N_e \gtrsim 10^8$ cm^{-3} typical of the solar corona. At much higher densities, $N_e \sim 10^{14}$ cm^{-3}, redistributive collisions can interrupt the two-step dielectronic process itself.

Therefore, we require dielectronic recombination from the metastable states as well as the ground. Secondly, we require final-state resolved data, i.e. we need to know the specific level that each two-step recombination ends-up in – the generalized collisional–radiative population rate equations govern the subsequent time-evolution of these states. (Incidentally, the first requirement imposes an additional requirement on the second, namely, that we now require dielectronic recombination into metastable parent final-states that lie above the ionization limit so that the collisional–radiative modelling recovers the Saha–Boltzman populations and ionization fractions in the high-density limit.) As we have already indicated, there are very many possible final states accessible to the dielectronic

recombination process which would seem to make for unacceptably large tabulations. However, it is not only impracticable, but unnecessary, to treat each final state in the same manner for the purposes of collisional–radiative modelling. The techniques of matrix condensation and projection reduce the effective number of high-lying states by the progressive bundling of representative states and project the full influence of the high-lying states down onto a fully-resolved low-lying set. (It is the low-level set which is the focus of detailed spectral analysis.) With this in mind, we can tailor our dielectronic recombination tabulations to reflect this situation.

Of course, many people have calculated both partial and total dielectronic recombination rate coefficients and it is impractical to list them all here. A useful starting point is the compilation of total recombination rate coefficients from the literature by Mazzotta et al. (1998) who then used this data to compute the coronal ionization balance for all elements up to Ni. When the results of ab initio calculations are not available then much use, and abuse, is made of the General Formula of Burgess (1965). Partial dielectronic recombination rate coefficients also abound in the literature in connection with the study of particular physical problems: for example, at low temperatures, where only a few autoionizing states contribute significantly (Nussbaumer & Storey 1983); satellite lines (e.g. Bely-Dubau et al. 1979); laser produced plasmas, where the electron density and/or charge state is high enough that the non-LTE populations are concentrated in a limited number of low-lying states (see e.g. Abdallah & Clark 1994).

We have found it helpful for application to prepare and handle dielectronic recombination data in a hierarchy of increasing sophistication which we call *baseline*, *level 1* and *level 2*. *Baseline* data are those produced using the Burgess general formula (GF), or with the techniques and state-selective programs associated with it. The generality of dielectronic data in use today are still from the GF. The background codes to the GF have a capability significantly beyond that of the GF, but are less well known. We return to these in more detail in Sect. 2.3. The *level 1* approach was introduced in the early "ninties" to support the GCR modelling of light elements such as Be, B and C. These species are used in "light-element strategies" for plasma facing wall components in fusion technology. For such elements, it is sufficient to use LS-coupled atomic structure and term population modelling. The relevant metastable populations in this case are terms such as C^{2+}(2s2p ^{3}P). The *level 2* approach, which is the main purpose of the present paper series, is concerned with the need to handle medium and heavy species in both fusion and astrophysics and to handle more extreme environments. In this approach, we aim to work with levels rather than terms and to use an intermediate coupling scheme, based on the use of the Breit–Pauli Hamiltonian (Badnell 1997).

There are several reasons why the *level 2* approach is now necessary: astrophysical spectral diagnostics tend to be based on levels rather than terms and the competition between autoionization and radiation makes it difficult to partition term-resolved dielectronic recombination data over levels; nuclear spin–orbit mixing is important even for low-Z ions, e.g. carbon, because only a weak mixing of LS-forbidden autoionization

rates with LS-allowed can give rise to "forbidden" autoionization rates that are comparable with the dominant radiative rates (see Nussbaumer & Storey 1984; Badnell 1988); as Z increases further then LS-forbidden radiative rates start to become significant; finally, dielectronic recombination via fine-structure transitions is completely absent in LS-coupling, giving rise to a large underestimate of the low-temperature dielectronic recombination rate coefficient in some iso-electronic sequences (see Savin et al. 1997).

The goal of this work is to calculate multi-configuration intermediate coupling dielectronic recombination rate coefficients from the (ground plus) metastable levels of an ion to all possible final states, resolved by level, and/or bundling, appropriate for generalized collisional–radiative modelling. We will cover elements applicable to astrophysics and magnetic fusion viz. He, Li, Be, B, C, N, O, F, Ne, Na, Mg, Al, Si, P, S, Cl, Ar, Ca, Ti, Cr, Fe, Ni, Zn, Kr, Mo and Xe. The first phase of the work will be the H- through Ne-like sequences. *Level 1* LS-coupling data for many elements of these sequences was calculated by Badnell (1991–92, unpublished) and incorporated into the atomic database part of the Atomic Data and Analysis Structure (ADAS) and is routinely drawn into the generalized collisional–radiative part of ADAS (see Summers 2003). So, we already have a clear pathway through to the complete utilization of the detailed *level 2* data that we will produce.

The second phase of the work will cover the Na-like through Ar-like sequences, piloted initially by further (*level 1*) LS-coupling calculations to extend the 1991–92 data. Note that ADAS uses year numbers for the introduction of new approximations bringing substantive contributions to the database. The LS-coupled work of Badnell above has the year number "93". The third phase will focus on the remaining sequences of particular elements of interest, e.g. Fe. Even with the compactification of the partial dielectronic recombination data, along the lines already indicated, full publication in a paper journal is impractical, and not especially useful. So, the entire data will be made available via the World Wide Web (see Sect. 5). The organization of the dielectronic data product follows the data format specifications of the ADAS Project. Dielectronic data are assigned to the data format *adf09* (Summers 2003).

The plan for the remainder of the paper is as follows: in Sect. 2.1 we review the generalized collisional–radiative approach encapsulated in ADAS and which influences our approach to handling dielectronic recombination data. In Sect. 2.2 we describe and justify the theoretical approach that we take to calculate *level 2* data. In Sect. 2.3 we review in some detail the essence of the Burgess approach. It will be shown that this remains of importance for a full exploitation of the new work, for example, as applied to the *l*-redistribution of autoionizing states. Also, it is necessary to assess the progress in the precision of new dielectronic data in comparison with the *baseline* data. In Sect. 3 we discuss the experimental situation for verifying dielectronic recombination data and the role of external fields. Some comparisons of results of our theoretical approach with high-resolution experimental results from storage rings are given. In Sect. 4 we address derived data and we present some illustrative comparisons of GCR effective coefficients obtained using *baseline*, *level 1* and *level 2* data from

dielectronic calculations. Also, we illustrate metastable-resolved ionization fractions. In Sect. 5 we give more detail of the organization of the database and the computational implementation of its production. We finish with a short summary.

2. Theory

2.1. Generalized collisional–radiative modelling

Consider ions X^{+z} of element X of charge state z. We separate the levels of X^{+z} into metastable levels X_ρ^{+z}, indexed by Greek indices, and excited levels, indexed by Roman indices. The metastable levels include the ground level. We assume that the excited levels X_i^{+z} are populated by excitation from all levels, ρ and j, of X^{+z}, by ionization from the metastable levels of X_μ^{+z-1} and recombination from the metastable levels of X_ν^{+z+1}. The dominant population densities of these ions in the plasma are denoted by N_ρ^z, N_μ^{z-1} and N_ν^{z+1}. The excited-state population densities, N_i^z, are assumed to be in quasi-static equilibrium with respect to the metastable populations. Thus,

$$0 = \sum_\sigma C_{i\sigma}^z N_\sigma^z + \sum_j C_{ij}^z N_j^z + \sum_\mu S_{i\mu}^{z-1} N_\mu^{z-1} + \sum_\nu R_{i\nu}^{z+1} N_\nu^{z+1}, \quad (1)$$

where C_{ij}^z are elements of the collisional–radiative matrix defined by

$$N_e C_{ij}^z = A_{j\to i}^r + N_e q_{j\to i}^e, \qquad j > i, \quad (2)$$

where N_e is the electron density, $q_{j\to i}^e$ is the electron-impact de-excitation rate coefficient and $A_{j\to i}^r$ is the spontaneous radiative rate, both for the $j \to i$ transition in the ion X^{+z}. The equivalent expressions for upward transitions ($j < i$) and for i and/or j replaced by a metastable index follow trivially. The diagonal element C_{ii}^z denotes the loss rate coefficient from the excited state i and is given by

$$C_{ii}^z = -\sum_{j \neq i} C_{ji}^z - S_i^z, \quad (3)$$

where

$$S_i^z = \sum_j S_{ji}^z \quad (4)$$

is the total ionization rate coefficient out of i. Finally, $S_{i\mu}^{z-1}$ is the partial ionization rate coefficient out of metastable μ and $R_{i\nu}^{z+1}$ is the partial recombination rate coefficient out of metastable level ν, both into level i of the ion X^{+z}. $S_{i\mu}^{z-1}$ includes contributions from both direct ionization and excitation-autoionization. $R_{i\nu}^{z+1}$ includes contributions from three-body, radiative and dielectronic recombination.

Solving for N_j^z, we have

$$
\begin{aligned}
N_j^z &= -\sum_{\sigma,i} (C^z)_{ji}^{-1} C_{i\sigma}^z N_\sigma^z - \sum_{\mu,i} (C^z)_{ji}^{-1} S_{i\mu}^{z-1} N_\mu^{z-1} \\
&\quad - \sum_{\nu,i} (C^z)_{ji}^{-1} R_{i\nu}^{z+1} N_\nu^{z+1} \\
&\equiv \sum_\sigma N_e \, {}^X\!\mathcal{F}_{j\sigma}^z N_\sigma^z + \sum_\mu N_e \, {}^I\!\mathcal{F}_{j\mu}^z N_\mu^{z-1} + \sum_\nu N_e \, {}^R\!\mathcal{F}_{j\nu}^z N_\nu^{z+1} \\
&\equiv \sum_\sigma {}^X\!N_{j\sigma}^z + \sum_\mu {}^I\!N_{j\mu}^z + \sum_\nu {}^R\!N_{j\nu}^z,
\end{aligned}
\quad (5)
$$

where $^{X}N_{j\sigma}^{z}$, $^{I}N_{j\mu}^{z}$ and $^{R}N_{j\nu}^{z}$ are the effective populations of j due to excitation, ionization and recombination from their respective metastables, and $^{X,I,R}\mathcal{F}_{j\beta}^{z}$ the corresponding coefficients. It is here that the connection with spectral analysis is made. The total emissivity in the line $j \to k$ is given by

$$\varepsilon_{j \to k}^{z} = N_{j}^{z} A_{j \to k}^{r}, \tag{6}$$

with the populations N_{j}^{z} given by Eq. (5). The corresponding photon emissivity coefficients are defined by

$$^{X,I,R}\mathcal{PE}\mathcal{C}_{\beta, j \to k}^{z} \equiv {}^{X,I,R}\mathcal{F}_{j\beta}^{z} A_{j \to k}^{r}, \tag{7}$$

respectively. Thus, the contributions to the total $j \to k$ emissivity from excitation, ionization and recombination are given by

$$^{X,I,R}\varepsilon_{j \to k}^{z} = N_{e} \sum_{\beta} {}^{X,I,R}\mathcal{PE}\mathcal{C}_{\beta, j \to k}^{z} N_{\beta}^{z, z-1, z+1}, \tag{8}$$

respectively.

The dynamic metastable populations N_{ρ}^{z} of X^{z} satisfy

$$\frac{1}{N_{e}} \frac{dN_{\rho}^{z}}{dt} = \sum_{\sigma} \left\{ C_{\rho\sigma}^{z} N_{\sigma}^{z} + \sum_{j} C_{\rho j}^{z} {}^{X}N_{j\sigma}^{z} \right\}$$

$$- \sum_{\sigma} \left\{ C_{\sigma\rho}^{z} N_{\rho}^{z} + \sum_{j} C_{\sigma j}^{z} {}^{X}N_{j\rho}^{z} \right\}$$

$$+ \sum_{\mu} \left\{ S_{\rho\mu}^{z-1} N_{\mu}^{z-1} + \sum_{m} S_{\rho m}^{z-1} {}^{X}N_{m\mu}^{z-1} \right\}$$

$$- \sum_{\nu} \left\{ S_{\nu\rho}^{z} N_{\rho}^{z} + \sum_{j} S_{\nu j}^{z} {}^{X}N_{j\rho}^{z} \right\}$$

$$+ \sum_{\nu} \left\{ R_{\rho\nu}^{z+1} N_{\nu}^{z+1} + \sum_{j} C_{\rho j}^{z} {}^{R}N_{j\nu}^{z} \right\}$$

$$- \sum_{\mu} \left\{ R_{\mu\rho}^{z} N_{\rho}^{z} + \sum_{m} C_{\mu m}^{z-1} {}^{R}N_{m\rho}^{z-1} \right\}$$

$$+ \sum_{\sigma} \left\{ Q_{\rho\sigma}^{z} N_{\sigma}^{z} + \sum_{m} S_{\rho m}^{z-1} {}^{R}N_{m\sigma}^{z-1} \right\}$$

$$- \sum_{\sigma} \left\{ Q_{\sigma\rho}^{z} N_{\rho}^{z} + \sum_{m} S_{\sigma m}^{z-1} {}^{R}N_{m\rho}^{z-1} \right\}$$

$$\equiv \sum_{\sigma} X_{CD:\sigma \to \rho}^{z \to z} N_{\sigma}^{z} - \sum_{\sigma} X_{CD:\rho \to \sigma}^{z \to z} N_{\rho}^{z}$$

$$+ \sum_{\mu} S_{CD:\mu \to \rho}^{z-1 \to z} N_{\mu}^{z-1} - \sum_{\nu} S_{CD:\rho \to \nu}^{z \to z+1} N_{\rho}^{z}$$

$$+ \sum_{\nu} \alpha_{CD:\nu \to \rho}^{z+1 \to z} N_{\nu}^{z+1} - \sum_{\mu} \alpha_{CD:\rho \to \mu}^{z \to z-1} N_{\rho}^{z}$$

$$+ \sum_{\mu} Q_{CD:\sigma \to \rho}^{z \to z} N_{\sigma}^{z} - \sum_{\sigma} Q_{CD:\rho \to \sigma}^{z \to z} N_{\rho}^{z}, \tag{9}$$

which defines the generalized collisional–radiative excitation (X_{CD}), ionization (S_{CD}), recombination (R_{CD}) and parent metastable cross-coupling (Q_{CD}) rate coefficients. (We note that $Q_{\rho\sigma}^{z} \equiv 0$ initially, by definition, then see Eq. (14) below.) This set of equations, together with those for N_{j}^{z}, are sufficient

to solve the low-level problem – those levels with principal quantum number $n \le n_{c}$, say. In the absence of dielectronic recombination, or at sufficiently high electron densities (e.g. $\gtrsim 10^{18}$ cm^{-3}, say, as found in laser-produced plasmas) then n_{c} can be small enough for this to be a complete solution since all higher levels are in collisional LTE, with a Boltzman population distribution. However, the presence of dielectronic recombination in low- to medium-density plasmas means that n_{c} can be prohibitively large (≈ 500, say).

We now consider a projection-condensation approach that allows for the effect of the high-level populations ($\overline{n} \equiv n > n_{c}$) on the low-level populations ($n \le n_{c}$) – see Summers & Hooper (1983) and Burgess & Summers (1969). We work in the bundled-n picture. Here the populations are grouped according to their parent level and principal quantum number. We assume that the high-level populations are in quasi-static equilibrium with the low-level populations and adjacent stage metastables. Thus, for each parent τ, the high-level populations (denoted by $\tau\overline{n}$) satisfy

$$0 = \sum_{n} C_{\tau\overline{n},\tau n}^{z} N_{\tau n}^{z} + \sum_{\overline{n}'} C_{\tau\overline{n},\tau\overline{n}'}^{z} N_{\tau\overline{n}'}^{z}$$

$$+ \sum_{\mu} S_{\tau\overline{n},\mu}^{z-1} N_{\mu}^{z-1} + \sum_{\nu} R_{\tau\overline{n},\nu}^{z+1} N_{\nu}^{z+1}, \tag{10}$$

which is of the same form as Eq. (1) for the low-level excited-states. Thus, the low-level populations satisfy equations of the same form as Eq. (9). This is a full solution for all levels, in the bundled-n picture. It includes direct couplings between the low-level populations (e.g. $n \to n'$) and indirect couplings via the high-level populations (e.g. $n \to \overline{n} \to n'$). However, we already have a description of the low-level problem in the fully-resolved picture, given by Eqs. (1) and (9). We can supplement these equations with the indirect couplings of the bundled-n picture, expanded over the low-level set using level weighting factors, ω_{ij}. This projection corresponds to solving Eqs. (1) and (9) with C, S, R and Q (including their appearance in Eq. (5)) replaced by C, S, $\mathcal{R}$ and Q where $C = C + {}^{ind}C$, $S = S + {}^{ind}S$, $\mathcal{R} = R + {}^{ind}R$ and $Q = Q + {}^{ind}Q$, where

$$^{ind}C_{\rho\sigma}^{z} = \omega_{\rho,\tau n} \omega_{\tau n',\sigma} \sum_{\overline{n},\overline{n}'} C_{\tau n,\tau\overline{n}'}^{z} (C^{z})_{\tau\overline{n}',\tau\overline{n}}^{-1} C_{\tau\overline{n},\tau n'}^{z}, \tag{11}$$

$$^{ind}S_{\nu'i}^{z} = \omega_{\nu n,i} \sum_{\overline{n},\overline{n}'} S_{\nu',\nu\overline{n}'}^{z} (C^{z})_{\nu\overline{n}',\nu\overline{n}}^{-1} C_{\nu\overline{n},\nu n}^{z}, \tag{12}$$

$$^{ind}R_{i\nu'}^{z+1} = \omega_{i,\nu n} \sum_{\overline{n},\overline{n}'} C_{\nu n,\nu\overline{n}'}^{z} (C^{z})_{\nu\overline{n}',\nu\overline{n}}^{-1} R_{\nu\overline{n},\nu'}^{z+1} \tag{13}$$

and

$$^{ind}Q_{\rho\sigma}^{z} = \omega_{\rho,\tau n} \omega_{\tau n',\sigma} \sum_{\overline{n},\overline{n}'} S_{\rho,\tau\overline{n}'}^{z-1} \left(C^{z-1} \right)_{\tau\overline{n}',\tau\overline{n}}^{-1} R_{\tau\overline{n},\sigma}^{z}. \tag{14}$$

Although we now have a complete solution in terms of the fully-resolved low-level and bundled-n high-level picture, one further step is of practical significance. In order to span a wide range of electron densities it is necessary to treat very large principal quantum numbers in order to reach the collision limit at low densities. It is not necessary to treat each n individually. Rather, a set of representative n-values can be used instead.

If $N_{\overline{n}}$ denotes the bundled-n populations for $\overline{n} = n_c + 1, n_c + 2, \ldots$, and $\mathcal{N}_{\overline{n}}$ denotes a subset of them, then the two are related via $N_{\overline{n}} = \omega_{\overline{n}\overline{\overline{n}}}\mathcal{N}_{\overline{\overline{n}}}$, where $\omega_{\overline{n}\overline{\overline{n}}}$ are the interpolation coefficients. Substituting for $N_{\overline{n}}$ into Eqs. (1) and (9) yields a condensed set of equations for $\mathcal{N}_{\overline{\overline{n}}}$ and the C, S, R and Q obtained from the condensed set of equations are identical in form to those obtained from the full set of equations.

We note here that we have made an assumption viz. that, following dielectronic capture, the autoionizing state is not perturbed by a further collision before it either autoionizes or radiates. This is not due to a limitation of ADAS but rather a choice that we have made (and defined within the *adf09* specification) so as to make the general collisional–radiative problem tractable over a wide range of electron densities. Working explicitly with autoionization and radiative rates and bound and non-bound states rather than partial dielectronic recombination rate coefficients and (mostly) bound states vastly increases the data requirements, in general. Although our collisional–radiative model goes over to the correct LTE limit at high electron densities, there is a density range ($\gtrsim 10^{16}$ cm^{-3}, found in laser-produced plasmas) where the levels of spectroscopic interest have non-LTE populations that are influenced by non-LTE populations of autoionizing levels that are themselves collisionally redistributed. We describe an approximate solution in Sect. 2.3 below.

We are now in a position to spell out our requirements of recombination data:
(i) we require recombination data from all metastable levels, not just the ground;
(ii) we require recombination data into particular final states;
(iii) we require the final-state to be level-resolved for $n \leq n_c$ and parent-level-resolved bundled-n for $n > n_c$;
(iv) parent metastable cross-coupling means that we require recombination into metastable autoionizing final states;
(v) we need only produce data for a representative set of $\overline{n}$.
The ADAS *adf09* data specification incorporates all of these requirements.

Finally, we note that use of total zero-density ground-state recombination rate coefficients is, in principle, quite unsafe for the collisional–radiative modelling of dynamic finite-density plasmas – see Burgess & Summers (1969), Summers & Hooper (1983), Badnell et al. (1993) and Sect. 4 below.

2.2. Dielectronic recombination rate coefficient modelling

We have already noted that the partial recombination rate coefficient (R_{iv}^{z+1}) includes contributions from three-body, radiative and dielectronic recombination. In ADAS, three-body recombination rate coefficients are obtained from electron-impact ionization rate coefficients, via detailed balance. This also ensures that the correct Saha–Boltzman limit is reached at high electron densities. Since three-body recombination is separate from dielectronic and radiative recombination, it is not necessary to consider it further. However, quantum mechanically, dielectronic and radiative recombination are indistinguishable processes which interfere with each other. In practice (see Pindzola et al. 1992), this interference is a very small effect

and can safely be neglected for our purposes. This is the independent processes approximation whereby dielectronic and radiative recombination can be considered separately and is the approach taken by the database aspect of ADAS. Separate data files exist for dielectronic (*adf09*) and radiative recombination (*adf08*) and they can be updated independently. Our focus is dielectronic recombination. Details of the ADAS data status for radiative recombination can be found in Summers (2003).

In the isolated resonance approximation, the partial dielectronic recombination rate coefficient α_{iv}^{z+1} from an initial metastable state v of an ion X^{+z+1} into a resolved final state i of an ion X^{+z} is given by (Burgess 1964)

$$
\alpha_{iv}^{z+1} = \left(\frac{4\pi a_0^2 I_H}{k_B T_e}\right)^{3/2} \sum_j \frac{\omega_j}{2\omega_v} e^{-E_c/(k_B T_e)}
$$
$$
\times \frac{\sum_l A_{j\to v, E_c l}^{a} A_{j\to i}^{r}}{\sum_h A_{j\to h}^{r} + \sum_{m,l} A_{j\to m, E_c l}^{a}}, \tag{15}
$$

where ω_j is the statistical weight of the ($N+1$)-electron doubly-excited resonance state j, ω_v is the statistical weight of the N-electron target state (so, $z = Z - N - 1$) and the autoionization (A^a) and radiative (A^r) rates are in inverse seconds. Here, E_c is the energy of the continuum electron (with orbital angular momentum l), which is fixed by the position of the resonances, and I_H is the ionization potential energy of the hydrogen atom (both in the same units of energy), k_B is the Boltzman constant, T_e the electron temperature and $(4\pi a_0^2)^{3/2} = 6.6011 \times 10^{-24}$ cm^3.

The effect of interacting resonances on dielectronic recombination has been investigated by Pindzola et al. (1992) and can safely be neglected, at least in the absence of external electric and magnetic fields (see Sect. 3 below). While autoionization rates can be determined (within the isolated resonance approximation) via the fitting of resonances calculated in a close-coupling approximation, or via the extrapolation of threshold close-coupling collision strengths using the correspondence principle, it is usual now to introduce a further approximation – that of using distorted waves, i.e. the autoionization rates are calculated via perturbation theory using the Golden Rule (Dirac 1930). This is the only approximation that we have made so far that may need to be reconsidered in certain cases. In low-charge ions, a perturbative distorted wave calculation may give inaccurate autoionization rates compared to those calculated in a close-coupling approximation. However, this only has a direct effect on the partial dielectronic recombination rate if the autoionization rates do not "cancel-out" between the numerator and denominator of (15) – typically, autoionization rates are orders of magnitude larger than radiative rates.

One could obtain (some) partial dielectronic recombination data from an *R*-matrix photoionization calculation, on making use of detailed balance, either in the absence of radiation damping (Nahar & Pradhan 1994) or with its inclusion (Robicheaux et al. 1995; Zhang et al. 1999). (One must take care not to double count the radiative recombination contribution in the modelling now.) However, this cannot provide us with a complete set of partial recombination rate coefficients since it is only

practicable to compute photoionization from (i.e. photorecom-bination to) a relatively low-lying set of states – up to $n \simeq 10$, say. Total recombination rates are obtained by supplementing the photorecombination data with high-n "close-coupling" di-electronic recombination rate coefficients calculated using Bell & Seaton (1985) or Hickman's (1984) approach. This is based on the radiative-loss term from a unitary S-matrix and does not, and cannot, resolve recombination into a particular final state, which is essential for collisional–radiative modelling. Indeed, even when summed-over all final states, errors can still re-sult. This has been demonstrated explicitly by Gorczyca et al. (2002) in the case of Fe^{17+}. They found that only the IPIRDW approach could reproduce the measured dielectronic recom-bination cross section of Savin et al. (1997, 1999) for high Rydberg states.

Thus, our initial goal is to generate complete data sets within the independent processes and isolated resonance us-ing distorted waves (IPIRDW) approximation. Subsequently, selective upgrades from R-matrix data may be made via, for example, the RmaX network which can be viewed as a pro-gression of the Iron Project (Hummer et al. 1993) and which is focusing on X-ray transitions – see, for example, Ballance et al. (2001). We note that while the Opacity Project (Seaton 1987) calculated a large amount of photoionization data, which in principle could be used for recombination (via detailed bal-ance), unfortunately, only total photoionization cross sections were archived, i.e. summed-over the final electron continuum, and so it is impossible to apply detailed balance and so it cannot be used as a source of recombination data.

We use the code AUTOSTRUCTURE (Badnell 1986, 1997; Badnell & Pindzola 1989) to calculate multi-configuration intermediate coupling energy levels and rates within the IPIRDW approximation. The code can make use both of non-relativistic and semi-relativistic wavefunctions (Pindzola & Badnell 1990). The low-n problem is no different from the one of computing atomic structure. The high-n problem requires some discussion. The mean radius of a Rydberg orbital scales as n^2 and so it rapidly becomes impossible to calculate an ex-plicit bound orbital (for $n > 20$, say) and some approximation must be made. We note that (Seaton 1983)

$$\lim_{n \to \infty} \left(\frac{\pi n^3}{2z^2} \right)^{3/2} P_{nl}(r) = F_{kl}(r)|_{k=0}, \tag{16}$$

where the bound orbitals (P_{nl}) are normalized to unity and the continuum orbitals (F_{kl}) to $\pi\delta(k - k')$, here $k^2 = E_c$(Ry). The approach taken in AUTOSTRUCTURE is to make use of (16) at finite n, i.e. to approximate the bound orbital by a suitably normalized zero-energy continuum orbital, for $n > 15 + l^2/4$ (evaluated in integer arithmetic). A further refinement is to evaluate the (true) continuum orbital for the incident electron at $E_c + z^2/n^2$ Rydbergs (instead of E_c) so as to maintain the same transition energy. (In the Bethe approximation, the free–free dipole acceleration integral is proportional to $\Delta\varepsilon^2$ times a slowly-varying-with-energy dipole-length integral, where $\Delta\varepsilon$ is the transition energy.) Actually, the true continuum orbital is calculated at about 15 energies per l and the one- and two-body bound–free integrals are interpolated at the required en-ergy, which is given by energy conservation. (The use of a

zero-energy continuum orbital means that long-range free–free integrals arise and these are treated using the techniques of distorted wave scattering theory, see Badnell 1983.) For each nl, AUTOSTRUCTURE reforms both the N- and ($N + 1$)-electron Hamiltonians and diagonalizes them (separately) to reform the rates. Only for H-like ions have we found it nec-essary to treat all l at the same time, and treat only each n sep-arately. Typically, each n is calculated explicitly until no new continua can open-up and then only a representative set of n, up to $n = 999$, is used. This approach avoids the extrapolation of low-n autoionization rates or, even worse, partial dielectronic recombination rate coefficients to high-n. Use of (16) is, in ef-fect, an interpolation since it is exact in the limit $n \to \infty$ and any error is bounded at the lowest-n by knowledge of the "ex-act" result obtained from using P_{nl} directly, rather than F_{kl}.

AUTOSTRUCTURE is implemented within ADAS as ADAS701. It produces the raw autoionization and radiative rates. To produce partial dielectronic recombination rate co-efficients, according to the prescription of Sect. 2.1, requires further non-trivial organization of the raw data. In particu-lar, radiative transitions between highly-excited Rydberg states are computed hydrogenically and added-in during a "post-processing" exercise with the code ADASDR, which is imple-mented with ADAS as ADAS702. Also, observed energies for the core and parent levels are used at this stage to ensure accurate positioning of the resonances and, hence, accurate low-temperature rate coefficients. ADASDR outputs directly the *adf09* file for use by ADAS. Separate *adf09* files are produced for different "core-excitations" ($n \to n'$), e.g. $1 \to 2$, $2 \to 2$ and $2 \to 3$ for Li-like ions. This enables selective upgrades of the *adf09* database.

2.3. Exploitation of the Burgess–Bethe approach

We are concerned with how the precise calculations de-scribed above relate to other calculations and, in particular, to those commonly used in astrophysics. Our *baseline* calcu-lation is based on the methodologies of Burgess, which rep-resent what can be achieved without recourse to the detail of the above sections. The Burgess GF itself was in fact a functional fit to extended numerical calculations. The associ-ated code, with extensions, we call the "Burgess–Bethe gen-eral program" (BBGP). It will be shown in this sub-section how the BBGP can be used to obtain a working model for the l-redistribution of doubly-excited states and, hence, provide a correction to accurate, but unredistributed, dielectronic data so as to model the dynamic part of the plasma microfield. Also, our *baseline*, calculated using the BBGP, will allow an assess-ment of the typical error that is present in the general dielec-tronic modelling in astrophysics to date.

In the LS-coupled term picture, introduce a set P of par-ent terms $\gamma_p {}^{2S_p+1}L_p$ of energy E_p relative to the ground parent term, indexed by p. Suppose that the excited parents are those with $p_{\min} \leq p \leq P$. The metastable parents, which are the initial metastables for recombination and the final parents on which the recombining excited nl-electron is built, are the sub-set $1 \leq p < p_{\min} = M$. Let p' denote an initial parent with the

incident electron denoted by $k'l'$. We wish to re-establish the expressions used by Burgess in his development and it is helpful to work in z-scaled dimensionless coordinates. Then, introducing $z_1 = z + 1$, the effective charge, the collision strength for a dipole excitation of $\gamma_p \, ^{2S_p+1}L_p$ to $\gamma'_p \, ^{2S_p+1}L'_p$, evaluated in the Bethe approximation, is given by

$$\Omega\left(\left(S_p L'_p\right) k'l', \left(S_p L_p\right) kl S L\right) = 48 \left((z_1 + 1)^2 / z_1^4\right)$$
$$\times \left(\frac{I_H}{\Delta\epsilon_{pp'}}\right)\left(\frac{(2S+1)(2L+1)}{2(2S_p+1)}\right) l_> \left\{\begin{matrix} L'_p & L_p & 1 \\ l & l' & L \end{matrix}\right\}^2$$
$$\times (2S_p+1)(2L'_p+1) f_{S_p L'_p \to S_p L_p} \left|\langle F_{k'l'} | \rho^{-2} | F_{kl}\rangle\right|^2 \quad (17)$$

in terms of the parent oscillator strength f, where $l_> = \max(l, l')$. For dielectronic recombination, it is convenient to express this in terms of the Einstein A-coefficient for the parent transition and to analytically continue the collision strength to negative energies for the kl electron, that is as $\kappa = k/z_1 \to i/n$. Formally, we identify a band of free-electron energies $dE/I_H = z_1^2 d\epsilon/I_H$, with the separation between n-shells $2z_1^2 I_H/n^3$, and let

$$\left|\langle F_{k'l'} | \rho^{-2} | F_{kl}\rangle\right|^2 d(\epsilon/I_H) \to (\pi/16)(\epsilon/I_H)^4 |\langle F_{k'l'} | \rho | P_{nl}\rangle|^2. \quad (18)$$

Then, the (dielectronic) resonance-capture cross section is given by

$$Q^c\left(\left(S_p L'_p\right) k'l', \left(S_p L_p\right) kl S L\right) d(E/I_H) \to \left(\frac{(z_1+1)^2}{z_1^4}\right)$$
$$\times \left(\frac{6\pi^2 a_0^3}{\alpha^4 c}\right)\left(\frac{\Delta\epsilon_{pp'}}{I_H}\right)\left(\frac{I_H}{\epsilon}\right)\left(\frac{(2S+1)(2L+1)}{2(2S_p+1)}\right) l_>$$
$$\times \left\{\begin{matrix} L'_p & L_p & 1 \\ l & l' & L \end{matrix}\right\}^2 \left(\frac{A^r\left(S_p L_p \to S_p L'_p\right)}{(z_1+1)^4}\right) |\langle F_{k'l'} | \rho | P_{nl}\rangle|^2. \quad (19)$$

The inverse (Auger) rate coefficient is obtained by invoking detailed balance as

$$A^a\left(\left(S_p L_p\right) nl S L \to \left(S_p L'_p\right) k'l'\right) = \left(\frac{(z_1+1)^2}{z_1^2}\right)\left(\frac{3}{2\alpha^3}\right)$$
$$\times \left(\frac{\Delta\epsilon_{pp'}}{I_H}\right)(2L'_p+1) l_> \left\{\begin{matrix} L'_p & L_p & 1 \\ l & l' & L \end{matrix}\right\}^2 \left(\frac{A^r\left(S_p L_p \to S_p L'_p\right)}{(z_1+1)^4}\right)$$
$$\times |\langle F_{k'l'} | \rho | P_{nl}\rangle|^2. \quad (20)$$

For the generalized collisional–radiative modelling of light element ions, it is convenient to use L-averaged doubly-excited levels, but still resolved by spin S, whereas the BBGP treatment uses SL-averaged levels. The corresponding Auger rates are then

$$A^a\left(\left(S_p L_p\right) nl S \to \left(S_p L'_p\right) k'l'\right) = \left(\frac{(z_1+1)^2}{z_1^2}\right)\left(\frac{1}{2\alpha^3}\right)\left(\frac{\Delta\epsilon_{pp'}}{I_H}\right)$$
$$\times \left(\frac{l_>}{(2l+1)}\right)\left(\frac{A^r\left(S_p L_p \to S_p L'_p\right)}{(z_1+1)^4}\right) |\langle F_{k'l'} | \rho | P_{nl}\rangle|^2, \quad (21)$$

in both cases. The matching resonance-capture coefficients are obtained by detailed balance, or by summing and averaging over the resolved expression for Q^c given above.

Turning to the radiative decay of the doubly-excited resonant states in the LS-resolved picture: the spontaneous emission coefficient, with a passive spectator in the nl shell, is given by

$$A^r\left(\left(S_p L_p\right) nl S L \to \left(S_p L'_p\right) nl S L'\right) = \left(2L_p + 1\right)\left(2L' + 1\right)$$
$$\times \left\{\begin{matrix} L'_p & L_p & 1 \\ L & L' & l \end{matrix}\right\}^2 A^r\left(S_p L_p \to S_p L'_p\right), \quad (22)$$

where $A^r(S_p L_p \to S_p L'_p)$ is the parent-core spontaneous transition probability. The L- and LS-averaged probabilities are both simply equal to $A^r(S_p L_p \to S_p L'_p)$. The BBGP method exploits the fact that, in the dipole case,

$$\frac{A^a}{A^r} = \frac{l_> |\langle F_{k'l'} | \rho | P_{nl}\rangle|^2}{2\alpha^3(2l+1)(z_1+1)^2 z_1^2}, \quad (23)$$

and efficient recurrence relations are available for the generation of hydrogenic bound–free radial integrals for all parameter values. It is clear that the Bethe approximation for the partial collision strengths can be substantially in error for $0 \le l \lesssim 2$. Burgess introduced correction factors for the lowest partial collision strengths, based-on a comparison with more sophisticated collision calculation results that were available at the time. More precisely, introduce

$$cor_l = \sum_{l'} \Omega\left(\left(S_p L'_p\right) k'l', \left(S_p L_p\right) k|_{=0}l\right) \Big/$$
$$\sum_{l'} \Omega^{\text{Bethe}}\left(\left(S_p L'_p\right) k'l', \left(S_p L_p\right) k|_{=0}l\right). \quad (24)$$

The general formula for zero-density total dielectronic recombination rate coefficients used a fixed-set of cor_l for all parent transitions. These were based-on parent $1s \to 2p$ transitions and it is the case that the inclusion of corrections is most significant for parent $\Delta n \ge 1$ transitions. To exploit the BBGP method beyond its use for the general formula, we must establish the population equations of the doubly-excited levels. For LS-averaged levels, the number densities expressed in terms of their deviations, $b_{p,nl}$, from Saha–Boltzmann, and referred to the initial parent p', are given by

$$N_{p,nl} = N_e N_{p'}^+ 8 \left[\frac{\pi a_0^2 I_H}{k_B T_e}\right]^{3/2} \frac{\omega_{p,nl}}{\omega'_p} e^{-E/(k_B T_e)} b_{p,nl}. \quad (25)$$

Then, in the BBGP *baseline* zero-density limit, with only resonant capture from the p' parent balanced by Auger breakup and radiative stabilization back to the same parent, we have

$$b_{p,nl} = \left(\frac{\sum_{l'} A^a(p, nl \to p'k'l')}{\sum_{l'} A^a(p, nl \to p'k'l') + A^r(p, nl \to p', nl)}\right). \quad (26)$$

In the extended BBGP program, we can also include resonant-capture from initial metastables other than the ground, dipole-allowed collisional redistribution between adjacent doubly-excited l-substates by secondary ion- and electron-impact, and losses by "alternate" Auger break-up and parent radiative

transition pathways. The population equations for the *l*-substates of a doubly-excited *n*-shell become

$$-\left(N_e q^e_{nl-1\to nl} + N^{z_1} q^{z_1}_{nl-1\to nl}\right) N_{p,nl-1}$$

$$+\left(\sum_{l'=l\pm1} N_e q^e_{nl\to nl'} + \sum_{l'=l\pm1} N^{z_1} q^{z_1}_{nl\to nl'}\right.$$

$$+ \sum_{p_1=1}^{p-1}\sum_{l'=l-1}^{l+1} A^a_{p,nl\to p_1,\kappa l'} + \left.\sum_{p_1=1}^{p-1} A^r_{p,nl\to p_1,nl}\right) N_{p,nl}$$

$$-\left(N_e q^e_{nl+1\to nl} + N_{z_1} q^{z_1}_{nl+1\to nl}\right) N_{p,nl+1}$$

$$= N_e \sum_{p_2=1}^{M}\sum_{l'=l-1}^{l+1} q^c_{p_2,\kappa l'\to p,nl} N_{p_2} + \sum_{p_1=p+1}^{P} A^r_{p_1,nl\to p,nl} N_{p_1,nl}. \quad (27)$$

These equations may be solved progressively downwards through the levels built on excited parents, terminating with levels built on the "final" ground and metastable parents. The calculations yield state-selective dielectronic recombination coefficients to levels built on each metastable parent, together with Auger rates, from levels built on metastables above the ground parent, to lower metastable parents. The results from the above solution, at zero density, we call *baseline* data.
We note some details of the implementation:

2.3.1. Collisional rates

Ion and electron *l*-redistributive cross sections are evaluated following the method of Pengelly & Seaton (1964). This is to be viewed as a very simplified treatment of the dynamic part of the plasma microfield associated with ions which move closer than their neighbours to the target. The quasi-static part of the ion microfield, which is approximately 1/3 of the total, is ignored at this level of analysis (see Sect. 3 for further discussion of field effects in an experimental context).

2.3.2. Energy levels

The energy differences $E_{p,nl\,S} - E_{p,nl\pm1\,S}$ are critical to the problem of doubly-excited-state redistribution. They are small, tending to zero at large *l*. Thus, the redistributive cross-sections are very large, remaining finite in the degenerate level limit only because of the finite radiative lifetime of the target (which is short for resonant states) or through screening of the projectile by nearest neighbours. For the $l = 0, 1, 2$ waves of the *n*-shell spectator electron, quantum defect expansions of the form $\mu_{p,nl\,S} = a_0 + a_1/n^2$ are usually available. For the higher l (> 2), the large number of energies required can be estimated more economically from the dipole polarizabilities, α^{pol}_p, of the parents, following Edlen (1964), as

$$E_{p,nl} = (z_1/n)^2[1 + 5.23504^{-4}(z_1/n)^2(n/(l+1/2)$$
$$+3/4)] + \alpha^{pol}_p(z_1/n)^4(3n^2 - l(l+1))/$$
$$(2n(l-1/2)l(l+1/2)(l+1)(l+3/2)). \quad (28)$$

Small-scale AUTOSTRUCTURE runs have been used to prepare these data for the *baseline*. We use two-term quantum defect expansions fitted at $n \to \infty$ and $n = 10$.

2.3.3. Bethe correction factors and radiative transition probabilities

For our comparisons, it is important that the inputs for the BBGP *baseline* calculations are consistent with the AUTOSTRUCTURE calculations for the *level 1* and *level 2* results. Small-scale AUTOSTRUCTURE runs have been used to prepare these inputs for the *baseline*. Low partial-wave collision strengths are now widely available (e.g. from AUTOSTRUCTURE), such that the cor_l can be prepared fairly easily. Within the ADAS Project, efficient subroutines for bound–free integrals and complete BBGP calculations are available together with sets of cor_l for the principal types of transitions. They are available to those for whom direct utilization of *level 1* and *level 2* data in full GCR modelling is not an option.

The results presented in this overview paper are illustrative only. Figure 1 contrasts zero-density total dielectronic recombination coefficients (α^{tot}_d) calculated in the GF and the BBGP *baseline* approximations with those of the *level 1* and *level 2* computations reported here. In particular, we note that *level 1* and 2 data are required to describe the recombination at low temperatures and that the *level 2* data provides a noticeable refinement over the *level 1* results. Figures 2a,b illustrate the partial recombination into *n*-shells and the population structure of the *l*-subshells of a representative doubly-excited *n*-shell. Figure 2a shows the very good convergence of BBGP to *level 1* data with increasing completeness of alternate Auger pathways. Figure 2b shows the effects of collisional redistribution at finite-density. A ratio of the sum over *l*-substates at a given density to that at zero density yields a BBGP finite-density adjustment factor of the total *n*-shell capture at zero density. The consistency between the BBGP, *level 1*, and *level 2* approaches allows us to use this adjustment factor on the *level 1* and *level 2* data. In advanced generalized collisional–radiative modelling, the BBGP finite-density redistributive code acts as an interface between the extraction of state-selective zero-density dielectronic data from the ADAS *adf09* database and its entry into the GCR population codes, corrected for finite-density doubly-excited state redistribution. Note also that routine semi-automatic comparisons as, illustrated here, provide the theoretical uncertainty estimate with which we can tag each dielectronic datum.

3. Experimental validation of dielectronic recombination data and the role of fields

The last decade has seen an enormous amount of experimental activity in the area of dielectronic recombination. In particular, heavy-ion storage rings coupled with electron-coolers have provided a wealth of data for partial dielectronic recombination. (The partial here is by the intermediate resonance state rather than the final state.) Most data is of the "bundled-*n*" form, but some *l*-resolution is possible for very low-lying states. The iso-electronic sequences studied range almost exclusively from H-like through to Na-like and nuclear charges have ranged between $Z = 2$ and 92. In all cases, in the absence of external fields, there is rarely any significant disagreement with theory, i.e. outside of the experimental uncertainty. A few
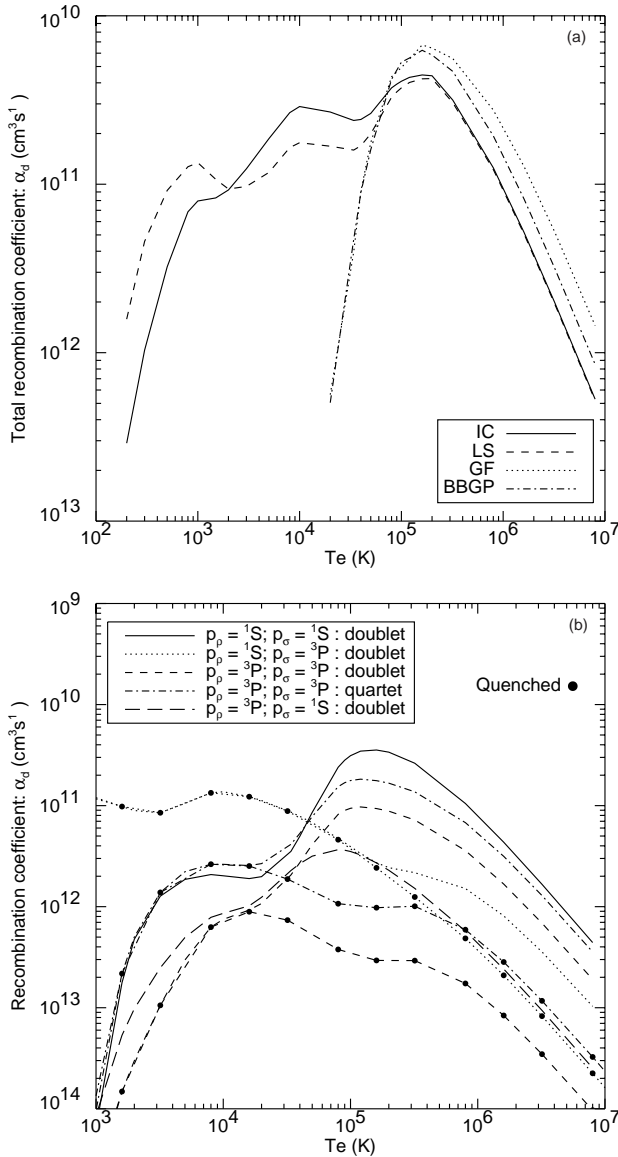
Fig. 1. The graphs contrast $\alpha_d^{(tot)}(p_\rho \to p_i \to p_\sigma)$ vs. T_e for the dielectronic recombination of O^{4+} ions in various approximations at zero density. **a)** $p_\rho = O^{4+}(2s^2 \ {}^1S)$, $p_\sigma = O^{3+}(2s^2 2p \ {}^2P)$: $\Delta n = 0$ and $\Delta n = 1$ intermediate parents included. The Burgess GF includes only the dipole $2s^2 \ {}^1S - 2s2p \ {}^1P$ and $2s^2 \ {}^1S - 2s3p \ {}^1P$ transitions. BBGP incorporates specific cor_l correction factors, energies which differ from those implicit in the GF, and the $3p - 3s$ alternative Auger channel. The *level 1* and *level 2* results include all allowed and non-allowed parent transitions within the $n = 2$ and $n = 3$ complexes. Note the low temperature extension which cannot be modelled with the GF and BBGP. The correct distinction and positioning of the key lowest resonances are possible only at *level 2*. **b)** $p_\rho = O^{4+}(2s^2 \ {}^1S)$ and $O^{4+}(2s2p \ {}^3P)$, $p_\sigma = O^{3+}(2s^2 2p \ {}^2P)$ and $O^{3+}(2s2p^2 \ {}^4P)$: *level 1* results separated by spin-system and final parent. Recombination from-and-to metastables cannot be handled by the GF. Excited-states built on the $2s2p \ {}^3P$ parent have a spin-change autoionization pathway. The *level 1* metastable-resolved totals do not include this loss. Within an LS-coupled GCR picture using *level 1* data, spin-breakdown Auger data is included explicitly in the GCR calculations for the correct linking of systems built on the $2s^2 \ {}^1S$ and $2s2p \ {}^3P$ parents. The relevant final-parent-changing Auger data is included in the *adf09* data file specification. For comparison with simpler treatments, totals including quenching of n-shells > 4 built on the $2s2p \ {}^3P$ parent are also shown.
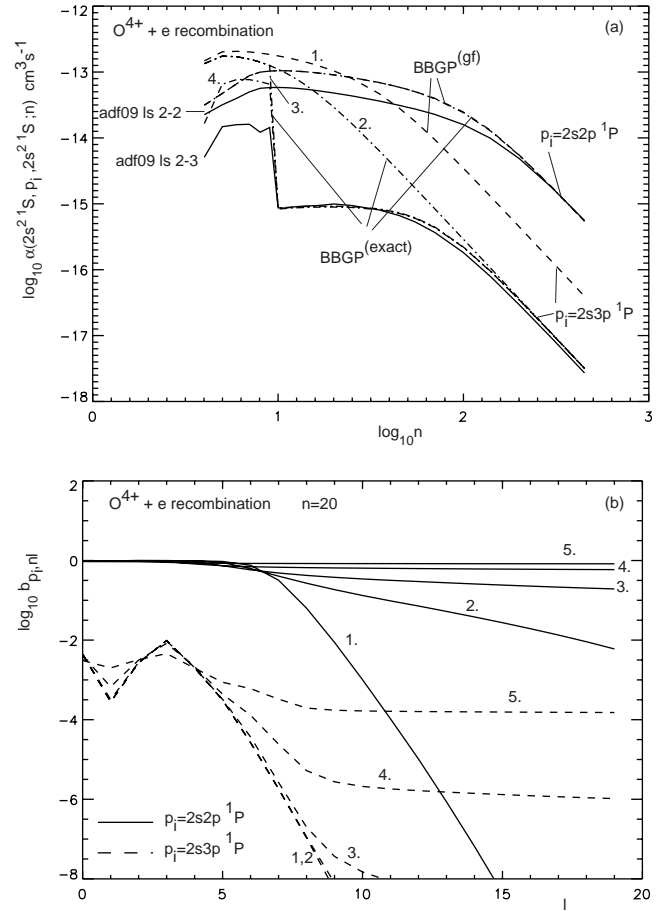

Fig. 2. O^{4+} recombination. **a)** Partial n-shell recombination coefficients: initial recombining metastable $2s^2 \ {}^1S$, intermediate excited parent p_i, final states $(2s^2 \ {}^1S)n$ with $p_i = 2s2p \ {}^1P$ and $2s3p \ {}^1P$. $T_e = 1.6 \times 10^6$ K, $N_e = N_p = 0$. BBGP${}^{(gf)}$ indicates use of standard cor_l matching the GF, BBGP${}^{(exact)}$ indicates use of specific cor_l. For the $\Delta n = 0$ case, BBGP${}^{(gf)}$ and BBGP${}^{(exact)}$ are superposed. $\Delta n = 1$ cases: 1. no alternative Auger channels, GF cor_l; 2. no alternative Auger channels, specific cor_l; 3. $2s3p \ {}^1P - 2s3s \ {}^1S$ alternative Auger channel, specific cor_l; 4. as before and $2s3p \ {}^1P - 2s2p \ {}^1P$ alternative Auger channel, specific cor_l. **b)** $b_{p_i,nl}$ factors for doubly-excited states of O^{3+} relative to O^{4+} $2s^2 \ {}^1S$ for $p_i = 2s2p \ {}^1P$ and $2s3p \ {}^1P$, $n = 20$, $T_e = 10^6$ K, $N_e = N_p$, plasma $Z_{eff} = 1$. Cases: 1. $N_e = 10^{10}$ cm^{-3}; 2. $N_e = 10^{12}$ cm^{-3}; 3. $N_e = 10^{13}$ cm^{-3}; 4. $N_e = 10^{14}$ cm^{-3}; 5. $N_e = 10^{15}$ cm^{-3}. Note the alternative Auger channel reduction for the $p_i = 2s3p \ {}^1P$ graphs.

of the more recent, typical, comparisons between experiment and the results of IPIRDW calculations include: Böhm et al. (2002), Savin et al. (2002a,b), Brandau et al. (2002). In Fig. 3, we show representative comparisons of dielectronic recombination data for $O^{5+} + e^- \to O^{4+}$ and $Fe^{18+} + e^- \to Fe^{17+}$, calculated in the IPIRDW approximation with AUTOSTRUCTURE and which illustrates the level of accuracy that can be expected of the theoretical data.

One major area of uncertainty is the role of external fields on dielectronic recombination, and it is this more than anything that renders pointless efforts to compute (zero-density) field-free data to an accuracy of better than $\simeq 20\%$, say. It has long been known that the high Rydberg states that frequently

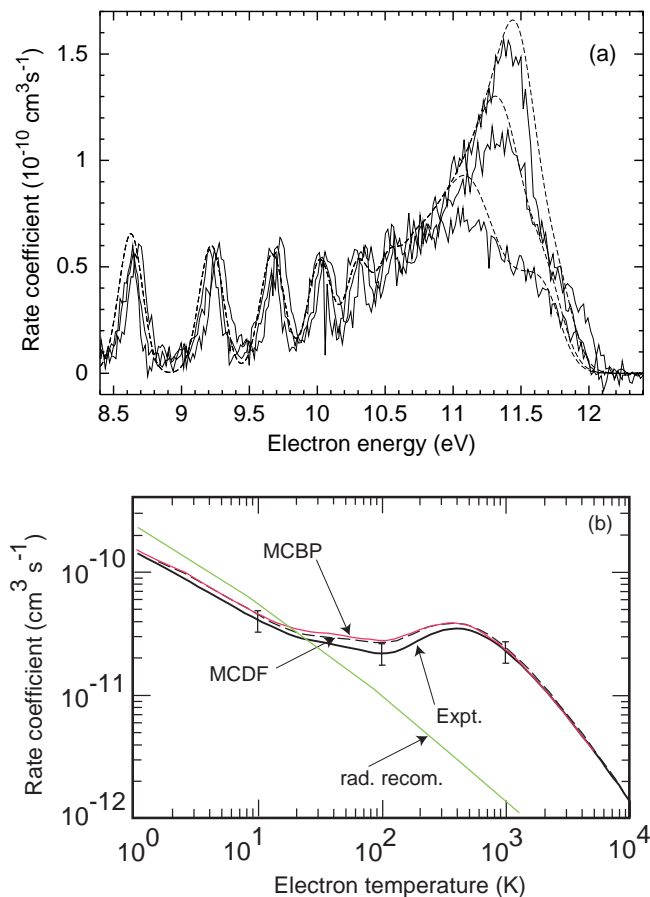**Fig. 3. a)** A theoretical reconstruction is shown of the observed dielectronic recombination resonances for the light ion $O^{5+} + e^- \rightarrow O^{4+}$. The measurement is from the CRYRING heavy-ion storage ring (Böhm et al. 2002). Note that the dielectronic recombination data from the methods described in Sect. 2.2 have been convoluted with the experimental velocity distribution, which has the units of a rate coefficient. The three pairs of curves correspond to three different beam energies which results-in three different cut-offs in the maximum principal quantum number detected. The experimental and theoretical data agree quite nicely. **b)** The Maxwellian dielectronic recombination rate coefficient for $Fe^{18+} + e^- \rightarrow Fe^{17+}$ is shown. The measurement (solid curve) is from the Heidelberg storage ring (Savin et al. 2002a) with an experimental error assessed as $\lesssim 20\%$. The theoretical IPIRDW results include the $1 \rightarrow 2$, $2 \rightarrow 2$ and $2 \rightarrow 3$ core excitations in the multiconfiguration Breit–Pauli (MCBP, dotted curve) and Dirac–Fock data (MCDF, dashed curve) with $n_{max} = \infty$. The worst deviation from experiments is $\lesssim 30\%$ (for the $3l3l'$ resonances) with a typical uncertainty $\lesssim 20\%$ for the direct state-selective coefficients to individual levels and for the total dielectronic rate coefficient. There is excellent agreement between the Breit–Pauli and Dirac–Fock results. The Breit–Pauli approach is used for our mass data production.

dominate the dielectronic recombination process can be Stark-mixed by weak electric fields (Burgess & Summers 1969), in particular the plasma microfield (Jacobs et al. 1976), and so increase the partial rate coefficients by factors of 2, or 3, or more, over a wide range of n. Recently, the picture has been further complicated by the discovery that magnetic fields, when crossed with an electric field, strongly affect the electric field

enhancement – by reducing it in most cases(see Robicheaux et al. 1997; Bartsch et al. 1999; Schippers et al. 2000; Böhm et al. 2001). While this suppression of the electric field enhancement is advantageous towards the use of field-free dielectronic recombination data, it is disadvantageous in terms of trying to compute field-dependent data for plasma modelling.

Previously, it appeared that a reasonable approach would be to use the values of the plasma microfield (which in turn depends on the plasma density) for the electric field strength for use in the generation of field dependent (i.e. density dependent) data as input to collisional–radiative modelling. This in itself ignored any further (e.g. external) electric fields that might be present in the plasma environment, beyond the plasma microfield. The recognition of the importance of magnetic fields as well makes a comprehensive solution to dielectronic recombination in a plasma a distant goal and partial data accurate to $\simeq 20\%$ as meaningful as necessary. Furthermore, field enhancement is sensitive to interacting resonances as well (see Robicheaux et al. 1998) unlike the field-free case. We do note again that high Rydberg states in a finite density plasma are brought into LTE by (electron) collisions. A preliminary study by Badnell et al. (1993) showed that the effect of the plasma microfield on the density-dependent effective recombination rate coefficient was suppressed by collisions driving high Rydberg states into LTE – larger values for the microfield, which lead to larger enhancements of the zero-density rate coefficient, corresponds to denser plasmas for which collisions drive more states into LTE.

4. Comparisons and assessments of the derived data

As described in Sect. 2.1, the emissivity and generalized collisional–radiative (GCR) coefficients depend inter alia on the fundamental dielectronic cross section data. There are two issues of concern in assessing these derived theoretical data, viz. the relative contributions to the effective coefficients coming from many different direct and indirect pathways and, secondly, estimation of the uncertainty in the theoretical data, which may be treated as a "working error" in the interpretation of spectral observations from plasmas.

For the effective photon emissivity coefficients ($\mathcal{PEC}$s), it is firstly to be noted that the relative importance of the contribution from excitation ($^X\mathcal{PEC}$) and recombination ($^R\mathcal{PEC}$) is directly proportional to the ionization balance fractional abundances of the (metastable) "driver" populations. The recombination part is most significant in transiently recombining plasmas and it is on this part only that we focus here. The partitioning of the collisional–radiative matrix described in Sect. 2.1 allows us to contrast the direct capture, capture coming via the complete set of resolved low-levels and capture via the high bundled-n quantum shells, which are treated by projection. The relative contributions depend differentially on density since the projection part is suppressed selectively at higher densities. Also, electron temperature and the recombining ion charge influence the relative importance of the dielectronic and radiative recombination contributions and the role of the more highly-excited levels. In Fig. 4, we show the main effects with some illustrative results from ADAS for
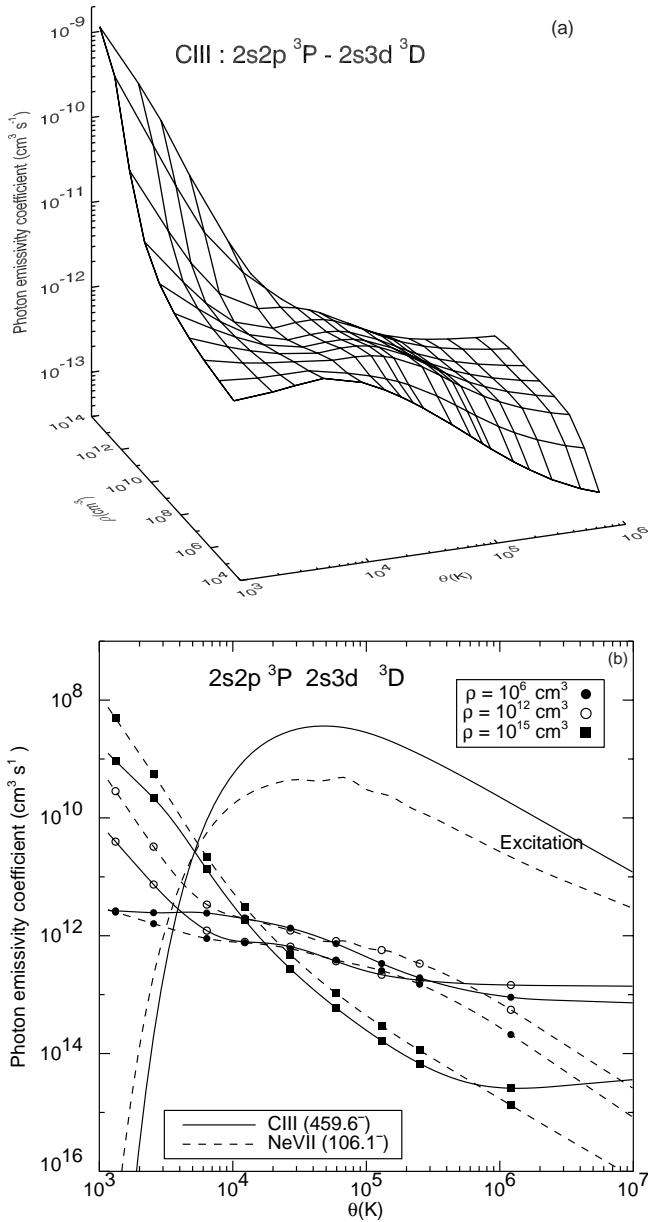
Fig. 4. a) Temperature and density dependence of the GCR $^R\mathcal{PEC}^z$ for the C III $2s2p\ ^3P - 2s3d\ ^3D$ multiplet at 459.6 Å driven by the $C^{3+}(2s\ ^2S)$ recombining ion. **b)** $^R\mathcal{PEC}^z$ for the C III $2s2p\ ^3P - 2s3d\ ^3D$ multiplet at 459.6 Å and Ne VII $2s2p\ ^3P - 2s3d\ ^3D$ multiplet at 106.1 Å, respectively. Additional curves contrast the corresponding $^X\mathcal{PEC}^z$s driven by the ground states of the recombined ions at $\rho = 10^{12}$ cm^{-3}. For comparison between isoelectronic systems, it is convenient to use the scaled electron temperature $\theta = T_e/z_1^2$ and scaled electron density $\rho = N_e/z_1^7$, where z_1 is the recombining ion charge (=3 and 7, respectively). Since the upper level is in the excited $n = 3$ shell, the cascading (projected) influence of higher levels is larger than for spectrum lines originating in the $n = 2$ shell. The low temperature behaviour is that of the radiative recombination process at low density, but rises to that of the collective three-body process at high density.

the C III $2s2p\ ^3P - 2s3d\ ^3D$ multiplet at 459.6 Å and the Ne VII $2s2p\ ^3P - 2s3d\ ^3D$ multiplet at 106.1 Å.

Figure 5 illustrates the main features of the generalized collisional–radiative recombination coefficients for
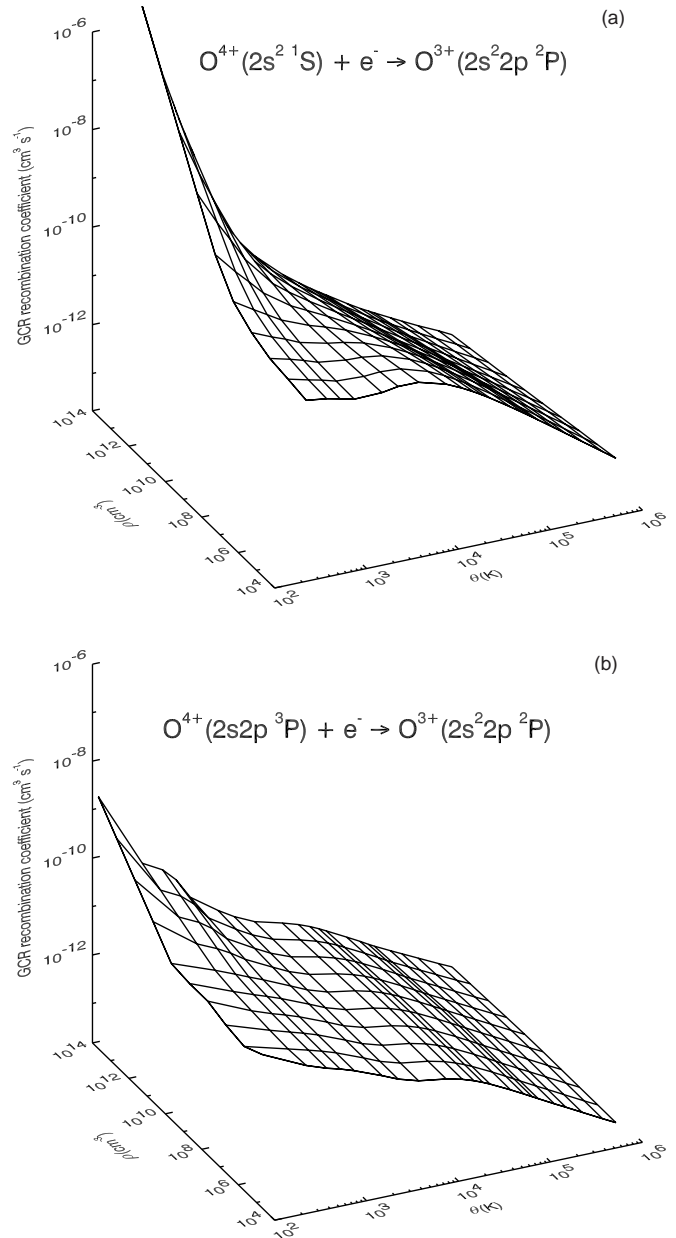
Fig. 5. a) $O^{4+} + e^- \rightarrow O^{3+}$ term-resolved GCR recombination coefficients that are driven from the $2s^2\ ^1S$ ground metastable of the O^{4+} ion as a function of electron temperature for a number of electron densities. The scaled electron temperature, θ, and scaled electron density, ρ, are used. **b)** $O^{4+} + e^- \rightarrow O^{3+}$ term-resolved GCR recombination coefficient driven from the $2s2p\ ^3P$ metastable of O^{4+}. The suppression of the coefficients compared with those of (a) is due to spin-breakdown alternative Auger channels. These must be included even in term-resolved GCR modelling.

$O^{4+} + e^- \rightarrow O^{3+}$. In the GCR term-resolved picture for light elements, there are four coefficients which are associated with the pairings of the $2s^2\ ^1S$ & $2s2p\ ^1S$ and $2s^22p\ ^2P$ & $2s2p^2\ ^4P$ metastable terms in the recombining and recombined systems, respectively. As the radiative and three-body processes are included, the low temperature and high density behaviours reflect these contributions. The finite-density suppression of the coefficient for the ground parent case and

the effect of alternative Auger channels are both pronounced and also depend on the ion charge. These effects require GCR modelling. The simpler stage-to-stage picture introduces a significant and, generally, unquantifiable error. It is to be noted that the intermediate-coupled dielectronic recombination data of this project also sustains production of fine-structure-resolved metastable GCR coefficients appropriate to medium- and heavy-weight elements.

The present paper's main concern is with ensuring the quality and completeness of dielectronic data for plasma modelling and not with all the consequential modelling of populations and ion distributions in plasmas. There are, however, two points to draw attention to. Firstly, it is well known that dielectronic recombination shifts equilibrium ionization balance fraction curves to higher temperatures. This is most pronounced for the ions with one or two electrons outside of closed shells and produces a characteristic "piling-up" of these stages. It is also these ion fractions which show most markedly the effect of finite density reduction of the collisional–radiative coefficients. This cannot be ignored for moderately ionized systems in plasmas with $N_e \gtrsim 10^{10}$ cm^{-3}. These effects are shown in Fig. 6 for oxygen. Secondly, most plasma transport models work only with whole ionization stage populations. The present work, however, sustains the metastable-resolved GCR picture. GCR coefficients and ionization balance fractional abundances must be bundled back to the ionization stage for such models, at the expense of precision. Figure 6b illustrates the resolved picture for the beryllium-like ionization stage of oxygen. The simplest bundling strategy imposes equilibrium fractions on the metastable populations relative to the ground, as is used for the stage-to-stage fractional abundances in Fig. 6a.

Modern good practice requires an estimate of uncertainty in derived theoretical data so that meaningful deductions can be drawn from the comparison with observations. It is unfortunately the case that most theoretical dielectronic data has no error associated with it. Because of the relative complexity of dielectronic recombination and the many contributions, agreements between different theories and with observations sometimes appear fortuitously and do not reflect the underlying reliability (see Savin et al. 2002a). For the present derived GCR coefficients and $^R\mathcal{PEC}$, we outline our approach to procuring a relevant "working error".

In the ADAS project (Summers et al. 2002), a distinction is made between "locked" parameters, as distinct from "search" parameters, in the optimized fitting of models to observations. Search parameters return a fit uncertainty or confidence level, the locked parameters must carry an error with them. An effective rate coefficient is such a locked parameter. Its uncertainty, called the cumulative statistical error, is computed from the errors of the fundamental reaction rates as follows: Monte Carlo samples are made of all the individual reaction coefficients, within their (assumed) independent Gaussian uncertainty distributions, and the derived coefficient calculated. The process is repeated many times until statistics are built up. The accumulated results are fitted with a Gaussian variance.

The key issue then is the starting point of uncertainties in the fundamental component dielectronic coefficients. The BBGP codes described in Sect. 2.3 have been arranged
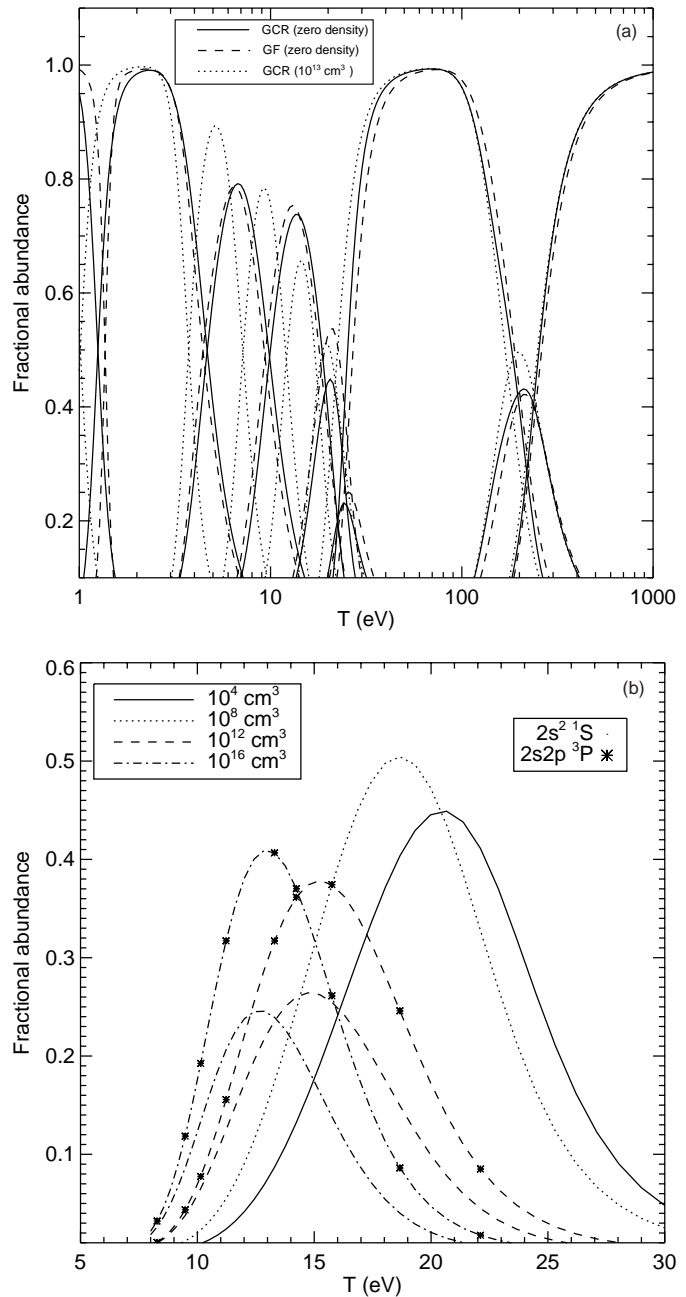

Fig. 6. a) Behaviour of the ionization balance fractional abundances for oxygen as a function of electron temperature and density. The balance is also shown using the GF for the dielectronic contributions. The same effective ionization rate coefficients were used in all three curve sets, but are not considered further here. The (*level 1*) GCR results are shown as a stage-to-stage balance, but originating from a true GCR metastable-resolved calculation. The metastable fractions are combined by weighting with their equilibrium fractions as determined by a low-level population balance. Note the potential confusion between differences due to the use of a low precision zero-density dielectronic calculation, such as the GF, and those due to finite-density effects. A more complete and sophisticated approach to such metastables (extended also to ionization stages) is called "flexible partitioning" and will be the subject of a separate work. **b)** Beryllium-like ionization stage, O^{4+}, fractional abundances in the metastable term-resolved GCR picture. Curves are shown, therefore, for both the 2s^2 ^{1}S and 2s2p ^{3}P ground and metastable terms. (The metastable curves are completely suppressed at the lowest two densities.)
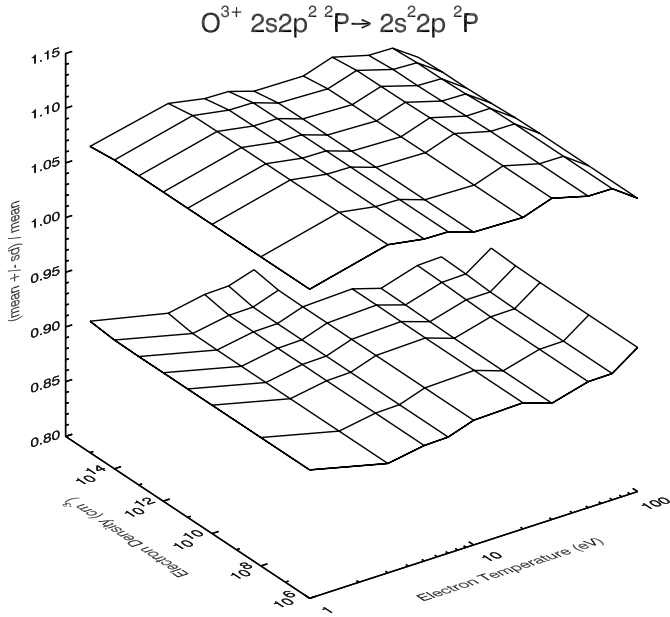
O^{3+} $2s2p^2$ $^2P \rightarrow 2s^22p$ ^2P

Fig. 7. Upper and lower cumulative statistical (± 1 standard deviation) surfaces for the $^R\mathcal{PEC}^z$ for the O IV $2s2p^2$ $^2P - 2s^22p$ ^2P multiplet at 554.4 Å. Note that projection has a substantial influence on the line emissivity and so its influence on the cumulative propagated error is significant. Projection and its error contribution is not included in the graph shown. $\mathcal{PEC}^z$ data are archived in ADAS data format *adf15*. The propagated "locked parameter" errors are available in *.err* files paralleling the *.dat* files for use in plasma modelling.

to generate *adf09 baseline* files. Such a file is differenced with the matching *level 1* file to provide an error estimate for the *baseline* values and may be stored in a *.err* file exactly paralleling the naming of the actual *.dat* file. In like manner, the *level 1* file may be differenced with the *level 2* file (averaged-over fine-structure) to provide the *.err* file for *level 1*. We treat this also as a conservative error for *level 2*. It is emphasized that this is not a confident absolute error, but a (hopefully) helpful appraisal of the theoretical data. It is most appropriate for the *n*- and *nl*- shell bundled data. The experimental comparisons of the type discussed in Sect. 3 indicate that a minimum uncertainty $\simeq 20\%$ is appropriate for the term- and level-selective dielectronic data. Use of such *.err* files is not yet a common practice and its handling within a projection matrix framework is complex. $^R\mathcal{PEC}^z$ error surfaces are shown in Fig. 7 using the ADAS procedure, but propagating error only from the state-selective part. The full handling of error will be treated in a separate paper.

5. Structure and access to the database

The complete set of dielectronic recombination data (both "partial" and "total") will be publically available as *adf09* files from the Controlled Fusion Atomic Data Center at the Oak Ridge National Laboratory, USA (http://www-cfadc.phys.ornl.gov/data_and_codes). These data files
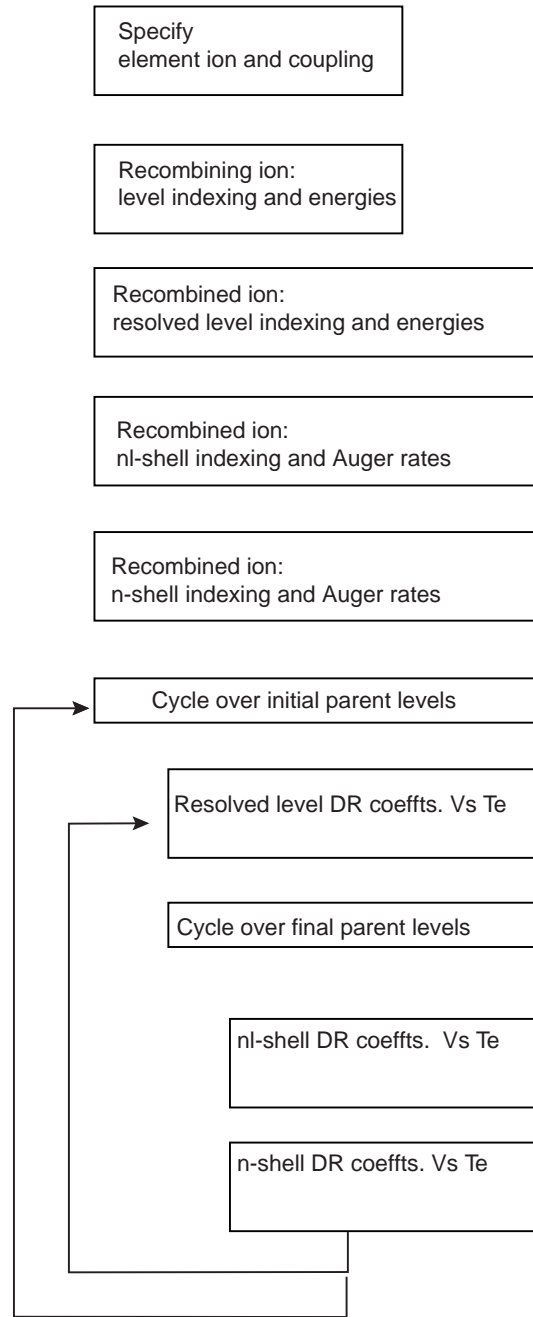

Fig. 8. Organization of data within the *adf09* format. *adf09* specifies both LS- and intermediate-coupled data organizations. In the LS-coupled case, the coefficients span resolved terms with valence electron up to $n = 7$; ≈ 40 representative *n*-shells up to $n = 999$. In the intermediate-coupled case, the coefficients span resolved levels with valence electron up to $n = 7$; all *nl*-shells up to $n = 10$; ≈ 40 representative *n*-shells up to $n = 999$. The coefficients are tabulated at 19 scaled temperatures spanning from 10–10^7 K. Auger rates for ionization to alternate metastable parents for the set of *nl*-shell and *n*-shell spectators built on each parent-metastable are included for model completeness. The detailed specification is in Appendix A of the ADAS User's Manual (Summers 2003).

are simple ascii text in a formatted organization. The layout differs slightly between the *level 1* LS-coupled and *level 2* intermediate-coupled forms. Figure 8 summarizes
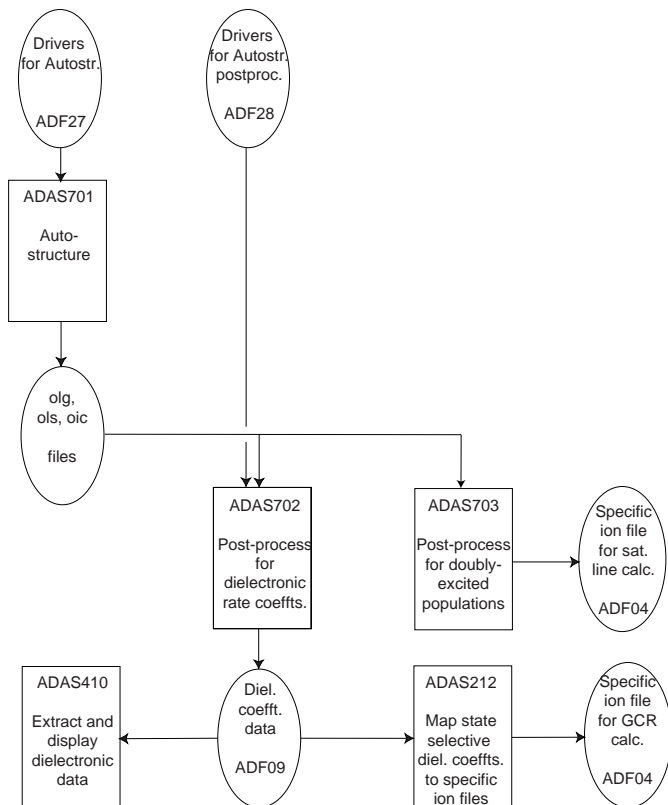
Fig. 9. ADAS code organization for production of the complete set of dielectronic data. ADAS701 is the AUTOSTRUCTURE code. The ADASDR post-processor code, ADAS702, prepares the level-resolved, bundled-*nl* and bundled-*n* partial recombination coefficient data according to the *adf09* format specification (Summers 2003). The code ADAS212 maps the level-resolved data onto the specific ion file class *adf04*. ADAS703 is an additional post-processor for dielectronic satellite line modelling and will be the subject of a separate paper. In a separate code chain (not shown here), ADAS807 prepares cross-referencing files to the bundled-*nl* and bundled-*n* data which are required for the very high-level population calculations and the evaluation of the projection matrices by ADAS204. The fully-configured *adf04* files, together with the projection matrices, are processed by ADAS208 which delivers the final generalized collisional–radiative (GCR) coefficients and effective emission coefficients.

the intermediate-coupled form. The document *appxa_09.pdf* of Appendix A of the ADAS user manual (available at: http://adas.phys.strath.ac.uk) provides the detailed description. This includes a summary of the sub-libraries and their current status, content of the data lines and the meanings of all parameters, together with some samples of the format. An example of a pathway to a member is */../adf09/jc00#li/jc00#li_ne7ic23.dat* which distinguishes the producer initials "*jc*", year number "00", recombining ion isoelectronic sequence "*li*", element "*ne*", coupling "*ic*" and parent $n = 2 \rightarrow n = 3$ transition group "23".

We have found it convenient to archive also the driver data sets, which initiate the *level 1* and *level 2* calculations, as other ADAS data formats (*adf27* and *adf28*). These have

pathways which parallel *adf09*. Various ADAS codes execute the primary calculations and the subsequent collisional–radiative modelling. The flow of calculation is summarized in Fig. 9.

6. Summary

We have described the goals and methodology behind a programme to calculate a comprehensive database of dielectronic recombination data for the collisional–radiative modelling of dynamic finite-density plasmas and illustrated its use in such environments. The first phase of the program covering H- through Ne-like sequences is under way and illustrative results, comparisons, and total (zero-density) rates will be the subject of a series of papers to follow in this journal: e.g., O-like ions, Zatsarinny et al. (2003) and Be-like ions, Colgan et al. (2003).

References

Abdallah, J., & Clark, R. E. H. 1994, J. Phys. B, 27, 3589
Badnell, N. R. 1983, J. Phys. B, 16, 3263
Badnell, N. R. 1986, J. Phys. B, 19, 3827
Badnell, N. R. 1988, J. Phys. B, 21, 749
Badnell, N. R. 1997, J. Phys. B, 30, 1
Badnell, N. R., & Pindzola, M. S. 1989, Phys. Rev. A, 39, 1685
Badnell, N. R., Pindzola, M. S., Dickson, W. J., et al. 1993, ApJ, 407, 91
Ballance, C. P., Badnell, N. R., & Berrington, K. A. 2001, J. Phys. B, 34, 3287
Bartsch, T., Schippers, S., Müller, A., et al. 1999, Phys. Rev. Lett., 82, 3779
Bell, R. H., & Seaton, M. J. 1985, J. Phys. B, 18, 1589
Bely-Dubau, F., Gabriel, A. H., & Volonté, S. 1979, MNRAS, 186, 405
Böhm, S., Schippers, S., Shi, W., et al. 2001, Phys. Rev. A, 64, 032707
Böhm, S., Schippers, S., Shi, W., et al. 2002, Phys. Rev. A, 65, 052728
Brandau, C., Bartsch, T., Hoffknecht, A., et al. 2002, Phys. Rev. Lett., 89, 053201
Burgess, A. 1964, ApJ, 139, 776
Burgess, A. 1965, ApJ, 141, 1588
Burgess, A., & Summers, H. P. 1969, ApJ, 157, 1007
Colgan, J., Pindzola, M. S., Whiteford, A. D., & Badnell, N. R. 2003, A&A, submitted (Paper III)
Dirac, P. A. M. 1930, Principles of Quantum Mechanics (OUP)
Edlèn, B. 1964, Handbuch der Physik 27 (Springer)
Gorczyca, T. W., Badnell, N. R., & Savin, D. W. 2002, Phys. Rev. A, 65, 062707
Hickman, A. P. 1984, J. Phys. B, 17, L101
Hummer, D. G., Berrington, K. A., Eissner, W., et al. 1993, A&A, 279, 298
Jacobs, V. L., Davis, J., & Kepple, P. C. 1976, Phys. Rev. Lett., 37, 1390
Judge, P. G., Hubeny, V., & Brown, J. C. 1997, ApJ, 475, 275
Lanza, A. F., Spadaro, D., Lanzafame, A. C., et al. 2001, ApJ, 547, 1116
Lanzafame, A. C., Brooks, D. H., Lang, J., et al. 2002, A&A, 384, 242
Mazzotta, P., Mazzitelli, G., Colafrancesco, S., & Vittorio, N. 1998, A&AS, 133, 403
Nahar, S. N., & Pradhan, A. K. 1994, Phys. Rev. A, 49, 1816
Nussbaumer, H., & Storey, P. J. 1983, A&A, 126, 75
Nussbaumer, H., & Storey, P. J. 1984, A&AS, 56, 293
Pengelly, R. M., & Seaton, M. J. 1964, MNRAS, 127, 165
Pindzola, M. S., & Badnell, N. R. 1990, Phys. Rev. A, 42, 6526

Pindzola, M. S., Badnell, N. R., & Griffin, D. C. 1992, Phys. Rev. A, 46, 5725

Robicheaux, F., & Pindzola, M. S. 1997, Phys. Rev. Lett., 79, 2237

Robicheaux, F., Pindzola, M. S., & Griffin, D. C. 1998, Phys. Rev. Lett., 80, 1402

Robicheaux, F., Gorczyca, T. W., Pindzola, M. S., & Badnell, N. R. 1995, Phys. Rev. A, 52, 1319

Savin, D. W., Bartsch, T., Chen, M. H., et al. 1997, ApJ, 489, 115

Savin, D. W., Kahn, S. M., Grieser, M., et al. 1999, ApJS, 123, 687

Savin, D. W., Kahn, S. M., Linkemann, J., et al. 2002a, ApJ, 576, 1098

Savin, D. W., Behar, E., Kahn, S. M., et al. 2002b, ApJS, 138, 337

Schippers, S., Bartsch, T., Brandau, C., et al. 2000, Phys. Rev. A, 62, 022708

Seaton, M. J. 1983, Rep. Prog. Phys., 46, 167

Seaton, M. J. 1987, J. Phys. B, 20, 6363

Summers, H. P. 2003, Atomic Data & Analysis Structure User Manual (Version 2.4) – http://adas.phys.strath.ac.uk

Summers, H. P., Badnell, N. R., O'Mullane, M. G., et al. 2002, Plasma Phys. Control. Fusion, 44, B323

Summers, H. P., & Hooper, M. B. 1983, Plasma Phys., 25, 1311

Zatsarinny, O., Gorczyca, T. W., Korista, K. T., Badnell, N. R., & Savin, D. W. 2003, A&A, submitted (Paper II)

Zhang, H. L., Nahar, S. N., & Pradhan, A. K. 1999, J. Phys. B, 32, 1459